CADAT 2025

The Second International Conference on Accessible Digital Agriculture Technologies

ISBN: 978-1-68558-328-6

October 26th - 30th, 2025

Barcelona, Spain

CADAT 2025 Editors

Pedro Gonçalves, Escola Superior de Tecnologia e Gestão de Águeda and Instituto de Telecomunicações, Portugal

CADAT 2025

Forward

The Second International Conference on Accessible Digital Agriculture Technologies (CADAT 2025), held between October 26th, 2025, and October 30th, 2025, in Barcelona, Spain, aimed at integrating cutting-edge Artificial Intelligence (AI) and Internet of Things (IoT) technologies into the agricultural sector. This conference focused on harnessing the power of AI and IoT to revolutionize farming practices, enhance productivity, and ensure sustainable food production for a growing global population. CADAT offered a comprehensive platform for researchers, practitioners, industry experts, and policymakers to exchange ideas, showcase innovations, and collaborate towards shaping the future of smart agriculture. Through interdisciplinary discussions and knowledge sharing, CADAT 2025 aimed to drive transformative change in the agricultural sector towards sustainability, efficiency, and resilience.

We take the opportunity to warmly thank all the members of the CADAT 2025 technical program committee, as well as all the reviewers. The creation of such a high-quality conference program would not have been possible without their involvement. We also kindly thank all the authors who dedicated much of their time and effort to contribute to CADAT 2025. We truly believe that, thanks to all these efforts, the final conference program consisted of top-quality contributions. We also thank the members of the CADAT 2025 organizing committee for their help in handling the logistics of this event.

We hope that CADAT 2025 was a successful international forum for the exchange of ideas and results between academia and industry for the promotion of progress in the field of accessible digital agriculture technologies.

CADAT 2025 Chairs

CADAT 2025 General Chairs
Sandra Sendra Compte, ORCID: 0000-0001-9556-9088, Universitat Politecnica de Valencia, Spain
Petre Dini, IARIA, USA/EU

CADAT 2025 Steering Committee
Chase Q. Wu, New Jersey Institute of Technology, USA
Khelifa Benahmed, ORCID: 0000-0001-8334-720X, Tahri Mohamed University – Bechar, Algeria
Antonio Javier Garcia-Sanchez, Universidad Politécnica de Cartagena, Spain
Jaime Lloret Mauri, Universitat Politecnica de Valencia, Spain
Zorica Srđević, University of Novi Sad, Serbia
Mohammed Ezziyyani, Université Abdelmalek Essaâdi, Morocco
Carlos Kamienski, Federal University of ABC (UFABC), Brazil

CADAT 2025
Committee

CADAT 2025 General Chairs

Sandra Sendra Compte, ORCID: 0000-0001-9556-9088, Universitat Politecnica de Valencia, Spain
Petre Dini, IARIA, USA/EU

CADAT 2025 Steering Committee

Chase Q. Wu, New Jersey Institute of Technology, USA
Khelifa Benahmed, ORCID: 0000-0001-8334-720X, Tahri Mohamed University – Bechar, Algeria
Antonio Javier Garcia-Sanchez, Universidad Politécnica de Cartagena, Spain
Jaime Lloret Mauri, Universitat Politecnica de Valencia, Spain
Zorica Srđević, University of Novi Sad, Serbia
Mohammed Ezziyyani, Université Abdelmalek Essaâdi, Morocco
Carlos Kamienski, Federal University of ABC (UFABC), Brazil

CADAT 2025 Technical Program Committee

Abdelkader Adla, University of Oran 1, Algeria
Ayda F. Aktas, Istanbul Technical University | Informatics Institute, Türkiye
Khelifa Benahmed, Tahri Mohamed University - Béchar, Algeria
Antonella Di Fonzo, Council for Agricultural Research and Economics | Research Centre for Policies and Bioeconomy, Rome, Italy
Mohammed Ezziyyani, Université Abdelmalek Essaâdi, Morocco
Laura Garcia, Universidad Politécnica de Cartagena, Spain
Antonio Javier Garcia-Sanchez, Universidad Politécnica de Cartagena, Spain
Saeid Homayouni, INRS, Centre Eau Terre Environnement (ETE/TENOR/GEO-AI) - Québec City, Canada
Satish R. Jondhale, Savitribai Phule Pune University, Pune, India
Carlos Kamienski, Federal University of ABC (UFABC), Brazil
Qinhuo Liu, Aerospace Information Research Institute (AIR) - Chinese Academy of Sciences, China
Jaime Lloret Mauri, Universitat Politecnica de Valencia, Spain
Vojtěch Merunka, Czech University of Life Sciences in Prague, Czech Republic
Simeon Ndoricimpa, Université du Burundi / Higher Institute of Management, Burundi
Lorenzo Palazzetti, University of Perugia, Italy
V. Pandiyaraju, VIT University, Chennai, India
Christina-Ioanna Papadopoulou, University of Western Macedonia, Kozani, Greece
Nikolaos Ploskas, University of Western Macedonia, Greece
Herminia Puerto-Molina, Centro en Investigación Agroalimentaria y Agroambiental (CIAGRO) | Universidad Miguel Hernández, Spain
Luís Quinta-Nova, Polytechnic University of Castelo Branco, Portugal
Javier Rocher Morant, FoodUPV, Universitat Politècnica de València, Spain
Sandra Sendra Compte, Universitat Politecnica de Valencia, Spain
Zorica Srđević, University of Novi Sad, Serbia
Chase Q. Wu, New Jersey Institute of Technology, USA

Copyright Information

For your reference, this is the text governing the copyright release for material published by IARIA.

The copyright release is a transfer of publication rights, which allows IARIA and its partners to drive the dissemination of the published material. This allows IARIA to give articles increased visibility via distribution, inclusion in libraries, and arrangements for submission to indexes.

I, the undersigned, declare that the article is original, and that I represent the authors of this article in the copyright release matters. If this work has been done as work-for-hire, I have obtained all necessary clearances to execute a copyright release. I hereby irrevocably transfer exclusive copyright for this material to IARIA. I give IARIA permission or reproduce the work in any media format such as, but not limited to, print, digital, or electronic. I give IARIA permission to distribute the materials without restriction to any institutions or individuals. I give IARIA permission to submit the work for inclusion in article repositories as IARIA sees fit.

I, the undersigned, declare that to the best of my knowledge, the article is does not contain libelous or otherwise unlawful contents or invading the right of privacy or infringing on a proprietary right.

Following the copyright release, any circulated version of the article must bear the copyright notice and any header and footer information that IARIA applies to the published article.

IARIA grants royalty-free permission to the authors to disseminate the work, under the above provisions, for any academic, commercial, or industrial use. IARIA grants royalty-free permission to any individuals or institutions to make the article available electronically, online, or in print.

IARIA acknowledges that rights to any algorithm, process, procedure, apparatus, or articles of manufacture remain with the authors and their employers.

I, the undersigned, understand that IARIA will not be liable, in contract, tort (including, without limitation, negligence), pre-contract or other representations (other than fraudulent misrepresentations) or otherwise in connection with the publication of my work.

Exception to the above is made for work-for-hire performed while employed by the government. In that case, copyright to the material remains with the said government. The rightful owners (authors and government entity) grant unlimited and unrestricted permission to IARIA, IARIA's contractors, and IARIA's partners to further distribute the work.

Table of Contents

Advanced Statistical Analysis of Physiological and Spectral Traits for the Early Detection of *Xylella fastidiosa* in Almond Trees

Laura Teresa Martínez-Marquina [1,†], José Ramón Torres-Martín [2,3,†], José Manuel Velarde-Gestera [3], Miguel Román-Écija [4], Guillermo León-Ropero [4], José Luis Trapero-Casas [4], Juan Antonio Navas-Cortés [4], Mihaela I. Chidean [1], and Inmaculada Mora-Jiménez [1]

[1]Department of Signal Theory and Communications, Telematics and Computing Systems
Rey Juan Carlos University, Madrid, Spain
e-mails: laura.marquina,mihaela.chidean,inmaculada.mora@urjc.es
[2]International Doctoral School, Rey Juan Carlos University, Madrid, Spain
e-mail: jr.torres.2023@alumnos.urjc.es
[3]Department of Research and Innovation, Drimay Consultores S.L., Seville, Spain
e-mails: josetm, jmvelarde@drimay.es
[4]Institute for Sustainable Agriculture (IAS), Spanish National Research Council (CSIC), Córdoba, Spain
e-mails: mromanecija,jleon,jltrapero@ias.csic.es,j.navas@csic.es
[†]These authors contributed equally to this work

***Abstract*—*Xylella fastidiosa* (*Xf*) is one of the most aggressive vascular pathogens threatening woody crops, particularly almond trees, in the Mediterranean region. This paper presents a statistical framework for the early detection of *Xf* infection prior to the onset of visible symptoms, leveraging multitemporal physiological and spectral data collected at the leaf level. The approach integrates measurements from porometry, fluorometry, and spectrometry with a non-parametric bootstrap resampling method to identify traits that differentiate health states and reveal physiological responses linked to disease progression. Results reveal that *Xf*-infected trees, which later develop visible symptoms, exhibit significant differences in median values of both spectral indices and physiological variables compared to healthy and intermediate health groups. Grounded in real field data, this work contributes to data-driven plant health monitoring and precision agriculture, demonstrating the potential of combining physiological and spectral indicators for early, non-invasive diagnosis of vascular diseases in perennial crops. The findings support the development of predictive tools for timely disease detection and management in almond and olive orchards.**

***Keywords*-bootstrap-based non-parametric test; *leaf scorch*; *physiological indices*; *hyperspectral indices*; *precision agriculture*.**

I. Introduction

Almond (*Prunus dulcis*) is a crop of major economic and cultural importance in Mediterranean regions [1]. However, its cultivation is increasingly threatened by pathogens such as the vascular bacterium *Xylella fastidiosa* (*Xf*) [2][3] which has emerged as one of the most devastating pathogens in Europe. The bacterium colonizes and obstruct the xylem vessels, disrupting water transport and leading to symptoms (e.g., leaf scorching, branch dieback or canopy desiccation) and eventually plant death [4][5]. Early detection of the diseases caused by *Xf* is challenging due to the asymptomatic infections and latency of visual symptoms and the systemic nature of the infection, highlighting the need for more sensitive and non-invasive diagnostic approaches.

The need for improved in early detection strategies extend to other vascular pathogens affecting woody crops. For example, the highly virulent defoliating pathotype D of *Verticillium dahliae* (*Vd*) [6] showed early physiological stress signals in infected olive trees, such as changes in canopy temperature, chlorophyll fluorescence, and spectral indices, well before visual symptoms appeared, using airborne hyperspectral and thermal imaging [7]. Subsequent studies [8][9] refined this approach, proving that foliar temperature, chlorophyll content, and pigment-based indices could serve as early indicators of plant disease, with Machine Learning (ML) models to classify disease severity across multiple levels.

Based on prior findings, recent studies have extended the use of remote sensing and ML techniques to differentiate between *Xf* and *Vd* infection in tree host. Although both pathogens share aspects of their pathogenesis that lead to similar visual symptoms, such as canopy desiccation and leaf scorching, they induce distinct physiological responses in host plants. A study in 2021 [10] proposed a three-stage classification approach that combined hyperspectral and thermal traits with ML algorithms to discriminate between *Xf* and *Vd* infections in olive trees, achieving over 90% accuracy for both pathogens. Their findings showed that each pathogen follows divergent physiological pathways: *Xf* is more associated with chlorophyll degradation (mainly captured by the Normalized Phaeophytinization Index, NPQI), anthocyanin accumulation, and changes in photochemical reflectance indices (e.g., normalized Photochemical Reflectance Index, PRI_n), while *Vd* is characterized by alterations in carotenoid content and water stress indicators (e.g., Crop Water Stress Index, CWSI). Building on this work, [2][11] demonstrated that these pathogen-specific spectral signatures remain consistent across both olive and almond trees. In particular, NPQI and Solar-Induced Chlorophyll Fluorescence at 760 nm (SIF@760),

indicator of photosynthetic efficiency and physiological stress, were identified as key traits for detecting *Xf* in olives. In contrast, other indices such as PRI_n and Modified Carotenoid Reflectance Index centered at 700nm (CRI_{700M}) were found to be more relevant in almonds, underscoring the importance of host-specific physiological responses in disease detection models. Finally, [12] focused specifically on *Xf* in almond trees, proposing the integration of hyperspectral and thermal imagery with an epidemic spread model. Their method enhanced early detection of asymptomatic *Xf*-infected almond trees, achieving up to 59% accuracy. These results highlight the value of integrating plant physiological traits with spatial epidemiological models for large-scale monitoring.

In this study, we aim to identify early physiological indicators of *Xf* infection in almond trees, prior to the onset of visible symptoms. To this end, we analyse multi-temporal leaf-level data acquired through spectrometry, porometry and fluorometry. Using bootstrap-based statistical testing, we identify the most informative traits for discriminating health states over time. Our goal is to establish a foundation for predictive models that support early and non-invasive diagnosis of *Xf* in almond trees, with potential transferability to other woody crops affected by vascular pathogens.

The paper is organized as follows: Section II introduces the database, detailing the preprocessing steps and the instance labelling procedure. It also presents the statistical test employed to identify relevant variables Section III reports and discusses the results, while Section IV concludes the study and outlines directions for future research.

II. Materials and Methods

In this section, we describe the dataset used in the study and also detail the preprocessing procedure. We present the criteria for instance labelling based on visual symptoms and molecular diagnostics, along with the strategy adopted to ensure temporal consistency in label assignment. Finally, we introduce the statistical framework employed to identify the most informative variables for early infection detection.

A. Dataset. Labelling and Preprocessing

The dataset provided by IAS-CSIC includes data from 96 almond trees located in several commercial almond orchards on Mallorca Island (Balearic Islands, Spain). Each tree, identified by a unique ID, has four records corresponding to different measurement dates in 2024: May 15th, June 5th, June 25th, and July 15th. Measurements were taken from one or two branches per tree, depending on whether the tree showed visual symptoms of the disease in the previous crop season. If symptoms were present in 2023, two branches were measured in 2024; otherwise, only one branch was measured. All measured branches were tested for the presence of *Xf* using a molecular diagnosis based on the quantitative Polymerase Chain Reaction (qPCR) analyses [13].

Leaf-level spectral reflectance data were collected using the PolyPen RP410-UVIS (Photon Systems Instruments, Brno, Czech Republic), a portable spectroradiometer that captures reflectance across 246 discrete wavelengths ranging from 326.2 nm to 791.8 nm. These data were used to calculate several vegetation indices, including physiological traits such as pigment concentration, leaf structure, and photosynthetic activity, serving as potential indicators of plant stress related to vascular diseases. This approach follows established methodologies developed by the IAS-CSIC team [3][14][15], where spectral traits have proven useful for detecting early plant responses to vascular pathogens.

In addition to spectral data, we incorporated physiological parameters measured with the portable instrument LI-600 porometer/fluorometer (LI-COR Biosciences, Lincoln, NE, USA). This device measures stomatal conductance, leaf temperature, ambient humidity, and steady-state chlorophyll fluorescence (Fs), providing information on plant water status and dynamic photochemical activity. Together, these physiological traits complement spectral data. As a result, 43 variables, hereafter referred to as physiological traits, were preserved from the LI-600 for further analysis.

For the exploratory analysis, missing values were removed on a per-variable basis. Outliers in physiological traits, defined as values exceeding the mean ± 20 times the interquartile range (IQR), were imputed using the mean of the corresponding branch. Additionally, some hyperspectral measurements exhibited anomalous values across the entire spectral range for specific leaves; these were considered unreliable and similarly imputed using the branch-level mean.

All leaf-level observations were labelled according to the health status of their corresponding branch. Four mutually exclusive groups were defined based on a combination of three criteria: (i) visual symptoms observed at the measured branch, (ii) molecular diagnosis via qPCR [13] conducted during the final measurement in July, and (iii) overall health status assessed by using a severity score.

Initially, each branch was assigned a single label per time point, which was then applied to all leaf samples collected from that branch. Importantly, branches from the same tree could receive different labels depending on their individual condition. Thus, the four categories were defined based on expert knowledge and measurements taken in July, as follows: Label 0: Negative qPCR result, no visual symptoms, and no suspicion of disease (severity score = 0); Label 1: Branches with negative qPCR result, no visual symptoms, but suspected disease (severity score > 0); Label 2: Branches with positive qPCR result, but no visual symptoms, regardless of the severity score; Label 3: Branches presenting visual symptoms, regardless of the qPCR result.

Figure 1 (a) provides a schematic overview of the labelling procedure described above. Each row represents one of the four measurement dates, while each column corresponds to a single tree identified by its ID. In cases where two branches from the same tree were measured, both labels are displayed within the same cell, separated by a diagonal line. The figure uses a colour coding: green for Label 0; yellow for Label 1; orange for Label 2; red for Label 3. Cells without colour indicate not available data. This visual format illustrates the temporal

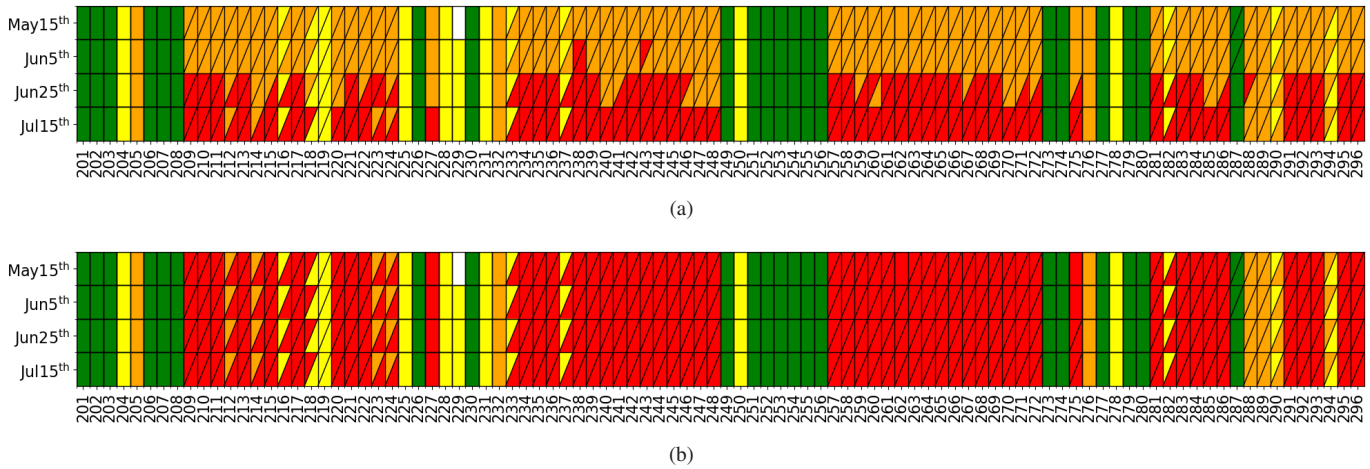

Figure 1. Label assignment scheme: (a) initial labelling based on visual symptoms, qPCR results in July, and overall health status based on a severity score; (b) retrospective labelling after backward propagation from the final measurement date (July 15th).

progression of the assigned labels and highlights variability within individual trees.

For subsequent analyses, a retrospective labelling approach was adopted: the label assigned at the final measurement (July 15th) was propagated backward to all earlier observations of the same branch. This approach aligns with the goal of identifying physiological and spectral markers linked to the final health status, ultimately aiming to develop predictive models for early-season detection of *Xf* infection. Figure 1 (b) displays this backward label propagation using the same structure and colour coding as in panel (a), where labels are redefined as follows:

- Label 0: Branches with neither visual symptoms nor suspected disease throughout the monitoring period (severity score = 0) and negative qPCR result in July.
- Label 1: Branches with no visual symptoms over time and negative qPCR result in July, but with suspected disease (severity score > 0).
- Label 2: Branches with no visual symptoms over time but a positive qPCR result in July, indicating *Xf*-infection.
- Label 3: Branches that eventually develop visual symptoms during the monitoring period.

To better illustrate the backpropagation labelling process, let us take tree ID 209 as an example. Neither of its branches showed visible symptoms on May 15^{th} or June 5^{th}, and were therefore initially assigned to Label 2 (Figure 1(a)). However, symptoms became evident on 25^{th} and July 15^{th}, leading to the retrospective assignment of Label 3 to the earlier dates, May 15^{th} and June 5^{th} (Figure 1(b)). This situation is not uncommon: branches ultimately assigned to Label 3 may not exhibit visible symptoms until the third or fourth measurement. Therefore, although they are retrospectively assigned to the most severe health status group from the first measurement, their actual condition may be milder in the early stages.

B. Statistical Analysis. Non-Parametric Difference Test

To identify which of the D variables are most discriminative in differentiating between the defined groups, a **non-parametric test for statistical differences** was employed. This approach requires the definition of a test statistic, denoted as $T(\cdot)$, which depends on the variable θ_d, where $d = \{1, \ldots, D\}$.

In our context, two test statistics $T(\cdot)$ were used: (i) the difference in medians between two groups, denoted as u and v (Eq. 1), and (ii) the difference in standard deviations between the same groups (Eq. 2).

$$T_1(\theta_d) = \text{median}(\theta_d)_u - \text{median}(\theta_d)_v \quad (1)$$

$$T_2(\theta_d) = \text{std}(\theta_d)_u - \text{std}(\theta_d)_v \quad (2)$$

A statistical comparison between groups was carried out by performing a hypothesis test for each variable. The aim was to determine whether the observed differences between groups for a given variable were statistically significant. The hypotheses for each test were defined as follows:

H_0 : There is no significant difference between groups with respect to θ_d

H_1 : There is a significant difference between groups with respect to θ_d

where H_0 and H_1 denote the *null* and *alternative* hypotheses, respectively.

To robustly estimate the value of the test statistic $T(\theta_d)$, particularly in scenarios with limited sample sizes and unknown population distributions, we employed a non-parametric **Bootstrap** resampling approach [16][17]. This approach involves repeatedly resampling the observed data with replacement to generate an empirical distribution of the statistic. The resulting estimate, $\hat{T}(\theta_d)$, closely approximates the true value, i.e., $\hat{T}(\theta_d) \approx T(\theta_d)$.

The bootstrap procedure involves generating multiple *re-samples* B^* of size m by randomly drawing observations from the original sample B of size n, with $m \leq n$. In this study, when comparing two groups, m was set to the size of the minority group to ensure balanced resampling. Importantly, resampling was performed *with replacement*, allowing individual observations to appear more than once

within a given B^*. This process was repeated N times, yielding a collection of N bootstrap estimates for the test statistic $T(\theta_d)$, denoted as $\{\hat{T}_1^*(\theta_d), \ldots, \hat{T}_N^*(\theta_d)\}$. These estimates form an empirical approximation of the sampling distribution of the statistic. Choosing a sufficiently large number of resamples N is essential to reduce variability in the bootstrap estimates and to obtain stable and reliable statistical inference.

Finally, to evaluate the statistical significance of the estimated test statistic $\hat{T}(\theta_d)$, we computed its empirical Confidence Interval (CI) based on the bootstrap distribution. The CI defines a range within which the true value of $T(\theta_d)$ is expected to lie with a specified probability, serving as a criterion for accepting or rejecting the null hypothesis. To construct the CI, a significance level α is defined, typically set to 0.05, which corresponds to a $100(1-\alpha)\%$ confidence level. This implies that the true value of $T(\theta_d)$ is expected to fall within the interval with probability approximately $1-\alpha$. Accordingly, the hypothesis test can be reformulated in terms of the CI as follows:

$$\begin{cases} H_0 : 0 \in CI(T(\theta_d)_{uv}) \\ H_1 : 0 \notin CI(T(\theta_d)_{uv}) \end{cases}$$

In this framework, if the CI does not include zero, there is sufficient evidence to reject H_0 in favour of H_1, indicating a statistically significant difference between the groups.

Based on this framework, the statistical test was applied at the leaf level. Each bootstrap instance corresponded to data from an individual leaf, allowing the analysis to capture within-branch variability in physiological and spectral traits. This procedure was performed independently for each of the D variables and across all four measurement time points. By treating each leaf as a distinct observation, the analysis achieves the highest granularity, enabling the detection of subtle group differences at the most localized scale.

III. Results and Discussion

The non-parametric bootstrap test was applied across all variables, including vegetation indices from the literature [3] and a broad set of physiological traits, to assess group-level differences. For each variable and time point, we evaluated differences in median values between health groups and also examined differences in variability (standard deviation) to capture physiological heterogeneity linked to disease progression.

To streamline the presentation, Figure 2 highlights hyperspectral and physiological traits that at least in two measurement dates showed significant differences between the two most contrasting health states, Label 0 (asymptomatic and qPCR-negative) and Label 3 (symptomatic). These comparisons are shown as the first CI for each variable. Additional CIs represent comparisons involving intermediate labels, which were also examined to evaluate their potential for early detection. Green CI indicate statistically significant differences, while red intervals indicate non-significant ones. The black dot indicates the median of each bootstrap distribution. While the Label 0 vs. Label 3 comparison was expected to yield the most pronounced differences, when comparing groups with intermediate labels (1 and 2), relevant differences also emerged. This reinforces the potential utility of these variables for early detection of physiological and spectral changes prior to symptom onset. Table I lists the variables whose CIs are displayed in Figure 2, along with their corresponding descriptions. Spectral indices ($MCARI_2$ to RGI) were computed from leaf-level hyperspectral reflectance data, while physiological traits (GSW to T_{leaf}) were obtained from direct measurements with the porometer/fluorometer.

A. Hyperspectral Indices

The results in Figure 2 (a) indicate that several spectral indices consistently differ in median values between the healthiest leaves (Labels 0 and 1) and those showing advanced symptoms (Label 3), particularly during the early measurements in May 15th and June 5th. This suggests that certain spectral indices may serve as early indicators of physiological disruption before visible symptoms appear. In contrast, differences in standard deviation were generally less conclusive (data not shown due to space constraints). The most notable variability differences were observed at the second time point (June 5th), particularly between the most severely affected groups (Labels 2 and 3). In some cases these differences persisted into later stages of the season, including late June and July, suggesting progressive physiological divergence as the infection advanced.

The indices DCabxc and TCARI, both associated with chlorophyll content, showed consistent differences between leaves labelled as 0 and those leaves labelled as 3 across all measurement dates. Additionally, both indices occasionally showed significant differences when comparing leaves labelled as 1 or 2 to those labelled as 3. Notably, TCARI has previously been identified as one of the most discriminative indices for detecting *Vd* symptoms in olive trees at both early and advanced stages, due to its sensitivity to chlorophyll degradation [9]. Similarly, in

Table I. Summary of variables.

Variable	Description
$MCARI_2$	Modified Chlorophyll Absorption Index
MSAVI	Modified Soil-Adjusted Vegetation Index
TVI	Triangular Vegetation Index
$MTVI_1$ $MTVI_2$	Modified Triangular Vegetation Indices
CTR_1	Carter Index
DCabxc	Reflectance Band Ratio Index
TCARI	Transformed Chlorophyll Absorption in Reflectance Index
T_O	TCARI / Optimized Soil-Adjusted Vegetation Index
VOG_1 VOG_2	Vogelmann Indices
$PRIM_3$	Photochemical Reflectance Index
G	Greenness Index
RGI	Red-Green Index
GSW	Stomatal conductance
GTW	Total conductance
$E_{apparent}$	Transpiration
VP_{leaf}	Leaf vapor pressure
$H2O_{leaf}$	Leaf H2O mole fraction
Fs	Minimum fluorescence in light
Fm'	Maximum fluorescence in light
$PhiPS_2$	Quantum efficiency in light
ETR	Electron transport rate
T_{leaf}	Calculated leaf temperature

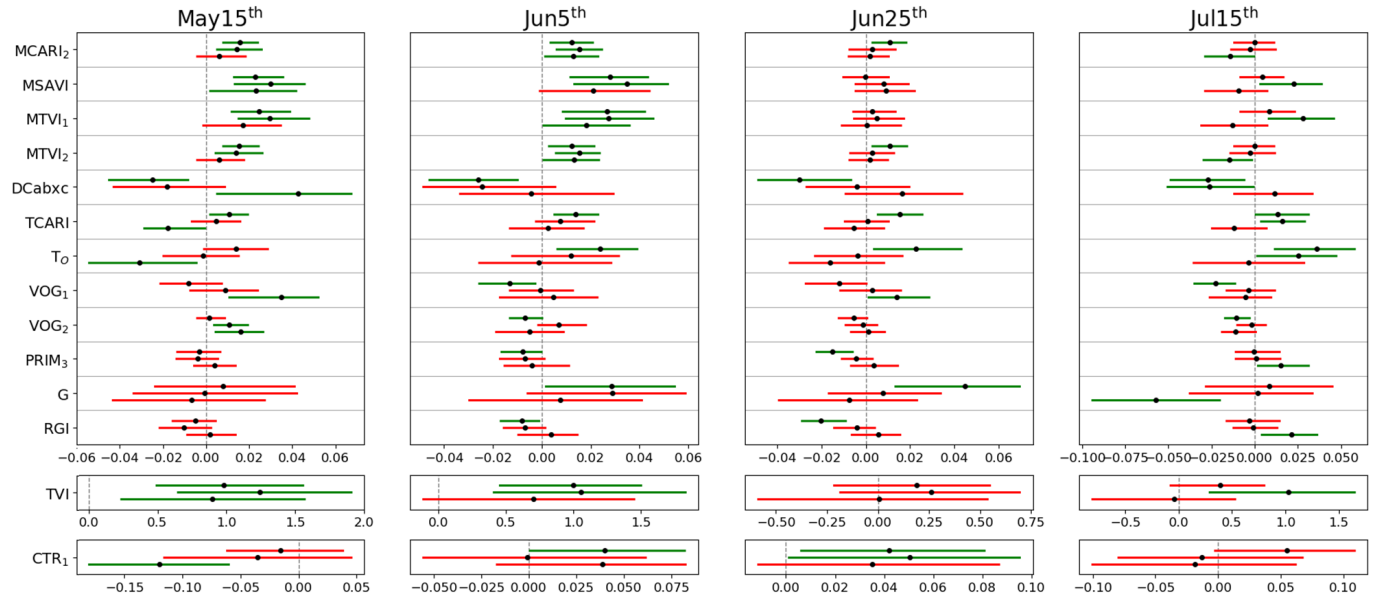

(a)

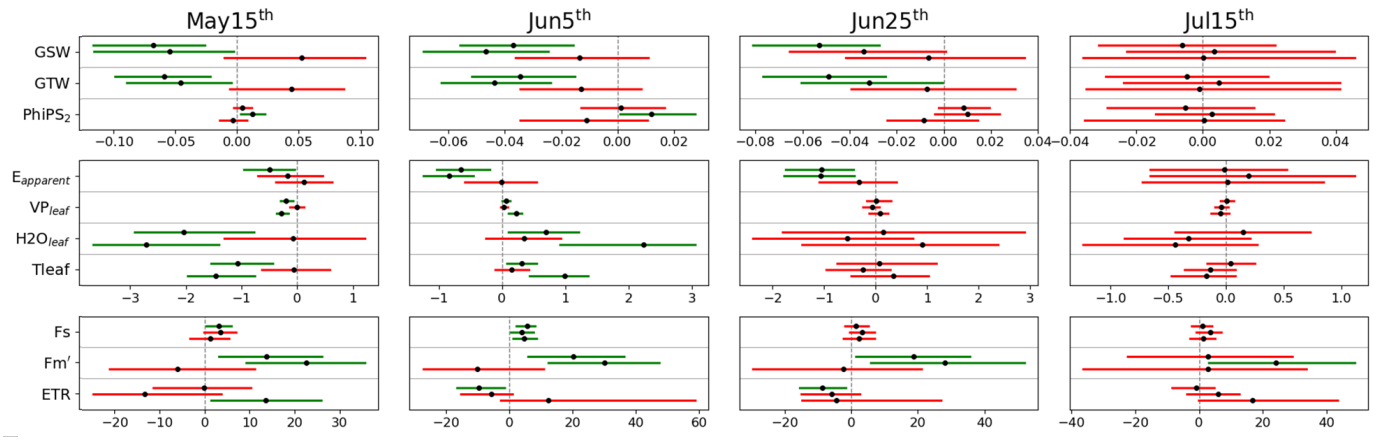

(b)

Figure 2. CI of bootstrap distributions for median differences between labelled groups pairs across time points: (a) spectral indices; (b) physiological traits. Each variable includes three CI, corresponding to comparisons between Label 0 vs. 3, Label 1 vs. 3, and Label 2 vs. 3, shown from top to bottom.

almond trees infected with *Xf*, TCARI also played a key role in remote sensing-based classification models, forming part of the index subset that most effectively distinguished symptomatic from asymptomatic trees [12]. The same study also highlighted the relevance of structural indices, such as MCARI, which are linked to leaf nutritional status. A progressive decline in MCARI values was reported as symptom severity increased, consistent with reduced nitrogen content in *Xf*-infected leaves. Our analysis aligns with these findings, showing statistically significant differences in MCARI between leaves from label group 0 and 3 during the first three measurement dates, and between Labels 1 and 3 during the first two. In all cases, the distribution shifted to the right, indicating lower MCARI values in the most affected group. In contrast, differences in standard deviation between groups were negligible, suggesting that overall variability in MCARI remained relatively stable regardless of *Xf* infection status.

Other structural indices, including TVI, $MTVI_1$, and $MTVI_2$, also showed significant median differences between leaves labelled as 0 and 1 and those labelled as 3, particularly during the first two measurement dates. In particular, when comparing label groups 1 and 3 at the second time point, TVI and $MTVI_1$ exhibited significant differences in dispersion, indicating increased variability in the physiological response of *Xf*-infected trees. Previous studies [9] have incorporated both TVI and $MTVI_1$ into discriminant analysis frameworks to classify *Vd* infection severity in olive trees. These indices significantly contributed to distinguish symptomatic from asymptomatic trees and to finer severity stratification. Further support is provided in [7], which identified these indices as part of a core set of structural traits frequently used in early disease detection models, likely due to their sensitivity to subtle canopy

 ISBN: ISBNFILL

structure changes associated with early pathogen infection.

Studies by [7] and [9] also identified Optimized Soil-Adjusted Vegetation Index (OSAVI), part of the soil-adjusted vegetation index family, as informative for plant health assessment. In our analysis (see Figure 2), we present results for MSAVI, which, like OSAVI, is derived from Normalized Difference Vegetation Index (NDVI) and uses the same spectral bands. However, MSAVI is often preferred in environments with sparse or discontinuous canopy cover and strong soil background influence, conditions typical of almond orchards. In our work, MSAVI consistently showed differences between the symptomatic reference group (Label 3) and the other label groups, particularly during the earlier measurement dates. This pattern supports the potential of soil-adjusted vegetation indices as effective early indicators of canopy-level physiological changes associated with pathogen infection.

Other notable pigment-related indices included T_O (TCARI/OSAVI), which estimates chlorophyll content while minimizing the soil reflectance effects, and the Vogelmann indices VOG_1 and VOG_2, which are sensitive to chlorophyll content and based on red-edge spectral bands. T_O has consistently been identified as one of the most responsive indices for detecting *Xf* infection in both olive trees [2][18] and almond trees [12]. In our analysis, T_O showed significant differences between leaves labeled as 0 and 3 during the June and July measurements, with higher values in leaves from healthy branches, indicating greater chlorophyll content. Similarly, the Vogelmann indices, previously reported for *Xf* detection in olive [2][18] and almond trees [12], showed differences between Labels 0 and 3 across several dates. Differences were also observed between intermediate groups (Labels 1 or 2) and group 3, highlighting the sensitivity of these indices to progressive chlorophyll degradation. Notably, VOG_1 showed significant differences in variability (standard deviation) only between the most severely affected groups (Labels 2 and 3) during early time points, with variability remaining relatively stable later in the season.

Figure 2 also includes the xanthophyll-related index $PRIM_3$, which, along with the G and RGI indices, demonstrated significant differences between leaves labelled 0 and those labelled 3 on June 5th and 25th. Furthermore, G and RGI also showed significant differences between groups 2 and 3 in the July measurement, highlighting their potential to detect progressive stages of *Xf* infection. The PRI and its variants, such as the normalized PRI_m, are well known for their effectiveness in identifying plant stress symptoms, including those caused by *Xf* [2]. These indices are closely linked to the xanthophyll cycle, which reflects changes in photosynthetic activity and efficiency under stress conditions [12].

Overall, these results confirm that several spectral indices, particularly those associated with pigment content and vegetation structure, can effectively discriminate between healthy and *Xf*–infected trees, even in asymptomatic stages. The strongest differences were observed between fully healthy leaves (Label 0) and infected and symptomatic leaves (Label 3). Significant differences among intermediate groups (Labels 1 and 2) further support the potential of these indices for early detection and large-scale monitoring of *Xf* infection.

B. Physiological plant traits

Figure 2 (b) shows the CI for physiological plant traits derived from porometer/fluorometer median differences between the healthiest (Label 0) and most affected (Label 3) trees, as well as the intermediate labelled groups against Label 3. Similar to spectral indices, certain physiological traits consistently differ between these groups, particularly in earlier measurement dates. This pattern suggests that these variables may be sensitive to early physiological alterations caused by *Xf* infection, even before visible symptoms appear. However, by the final measurement in July, these differences tend to diminish likely due to a general increase in thermal and water stress affecting all trees. This is supported by the relevance of temperature-based indices like the Crop Water Stress Index (CWSI) in *Xf* detection [7][9]–[12]. Under such uniform stress conditions, physiological responses among trees may converge, making it harder to distinguish between healthy and infected trees. It is plausible that trees labelled as 0 could recover post-stress, while those labelled as 3 may not, due to their compromised physiological state. Unlike these indices, the dispersion of variables across groups shows significant differences, particularly between Labels 0 and 3 in May and June. This highlights the potential of porometer/fluorometer-derived traits as early and sensitive indicators of *Xf* infection, though their discriminatory power may decrease under widespread environmental stress later in the season [10][11].

Conductance variables (GSW and GTW) exhibit significant differences in median values between the healthiest leaves (Labels 0 or 1) and the most affected ones (Label 3) at early stages, linking leaf health to conductance [12]. Interestingly, both conductance and transpiration, estimated by the $E_{apparent}$ variable, are higher in Label 3 leaves (potentially infected but still asymptomatic) than in healthy ones. This contrasts with reported findings that *Xf* infection typically reduces conductance and transpiration due to xylem blockage and impaired water transport [3]. This discrepancy may reflect a transitional infection phase, where physiological decline is not yet fully established or is masked by compensatory mechanisms [3]. Among the most affected groups (Labels 2 and 3), median values of conductance and transpiration (i.e., $E_{apparent}$) do not differ clearly. While conductance shows greater dispersion in May and June measurements than in the last measurement, transpiration variability does not differ significantly. These patterns suggest that early or asymptomatic stages of infection can produce variable physiological responses that may not always align with the typical decline reported in advanced stages [3][19].

The VP_{leaf} variable shows significant differences between leaves labelled 0 and 3, as well as between groups 2 and 3 in early stages. In May, the most affected leaves (Label 3) have higher CI values for vapour pressure, but this trend reverses in June. Vapour pressure deficit is recognized as an early indicator

of water stress caused by *Xf* infection [7][12][18]. Similarly, $H2O_{leaf}$ exhibit similar group differences as VP_{leaf}.

For fluorescence parameters, the healthiest leaves showed significantly higher median values of minimum (F_s) and maximum (F_m') fluorescence early in the season, with all group comparisons becoming significant by June. This aligns with previous findings that fluorescence is a sensitive indicator of *Xf* infection, typically decreasing as photosynthetic activity declines [12]. However, these differences fade as visual symptoms appear later in the season, and variability in fluorescence remains inconclusive. Another fluorescence-related variable, $PhiPS_2$, only showed significant differences between groups 1 and 3 during the first two measurement dates. In contrast, ETR values were higher in Label 3 leaves compared to Label 0 during the second and third time points.

Finally, leaf temperature T_{leaf} was significantly higher in group 3 compared to groups 0 and 2 in June, consistent with previous findings [2]. However, this trend reverses in the second measurement date, with T_{leaf} being higher in groups 0 and 2 than in group 3. At more advanced infection stages, significant differences in T_{leaf} are no longer observed between groups.

IV. Conclusion and Future Work

The results directly support the main objective of the study of identifying early physiological indicators of *Xf* infection in almond trees, prior to the onset of visible symptoms. Multitemporal leaf-level data, analyzed through non-parametric bootstrap testing, consistently revealed that both spectral and physiological traits can detect infection at early stages. Specifically, hyperspectral indices linked to pigment content (e.g., TCARI, DCabxc, MCARI) and structural traits (e.g., TVI, $MTVI_1$, MSAVI), along with physiological variables such as stomatal conductance, transpiration, vapour pressure, fluorescence, and leaf temperature, consistently distinguished healthy from infected trees in early stages.

These findings may suggest that physiological stress responses precede visible symptom development and can be captured through targeted measurements. Moreover, they align with recent evidence indicating that remote sensing traits, particularly fluorescence and thermal signals, enable accurate, large-scale, and early detection of *Xf*, supporting their use in disease monitoring and management. Interestingly, though differences were most pronounced in May and June, they tended to diminish by July. This likely reflects a general increase in thermal and water stress affecting all trees, which may mask infection-specific responses. It is plausible that healthy trees (Label 0) may recover after the stress period, whereas infected trees (Label 3) likely remain physiologically compromised. Although our analysis focused on variables showing statistically significant differences between the two most contrasting health states (Labels 0 and 3) across at least two time points, relevant differences also emerged among intermediate groups. This reinforces the diagnostic potential of the selected indicators and their applicability to early-stage detection.

This study represents an initial step toward developing a comprehensive framework for early *Xf* detection using spectral data acquired via proximal sensors. A limitation of this study is the small size in intermediate health groups (Labels 1 and 2), which may reduce the statistical power in comparisons involving these categories. To address this, future work will aim to improve dataset balance by increasing representation in these groups.

Given the complexity of *Xf* infections, further validation is essential. This includes defining threshold values for vegetation indices that reliably capture early physiological alterations. Additional research should refine trait selection, account for environmental variability, and validate findings across different crops and landscapes. Future efforts should also focus on integrating the identified physiological and spectral indicators into operational remote sensing workflows, as well as ML and spatial epidemiological models, to improve diagnostic accuracy and scalability. Expanding the use of multispectral and thermal sensors, along with optimized band selection, will be essential for developing cost-effective, real-time tools for disease surveillance and management.

Acknowledgement

This work has been partially supported by the Spanish Ministry of Science, Innovation and Universities through the CDTI with grant number EXP-00146371/MIG-20211037 (KODA-IPEC) and through the Spanish Research Agency with grant numbers PID2022-136887NB-I00 (POLIGRAPH) and PID2022-140786NB-C31 (LATENTIA), by Drimay Consultores S.L. with the Project F1285, and by the Community of Madrid through the 'Grants for the Hiring of Research Assistants from the Community of Madrid 2023', grant number PEJ-2023-AI/SAL-GL-28386.

References

[1] E. Spada *et al.*, "Economic Sustainability Assessment of Mediterranean Crops: A Comparative Life Cycle Costing Analysis", *Frontiers in Sustainable Food Systems*, vol. 6, p. 1 004 065, 2022.

[2] P. J. Zarco-Tejada *et al.*, "Divergent Abiotic Spectral Pathways Unravel Pathogen Stress Signals Across Species", *Nature Communications*, vol. 12, no. 1, p. 6088, 2021.

[3] P. J. Zarco-Tejada *et al.*, "Previsual Symptoms of Xylella Fastidiosa Infection Revealed in Spectral Plant-Trait Alterations", *Nature Plants*, vol. 4, no. 7, pp. 432–439, 2018.

[4] J. Rapicavoli, B. Ingel, B. Blanco-Ulate, D. Cantu, and C. Roper, "Xylella Fastidiosa: an Examination of a Re-Emerging Plant Pathogen", *Molecular Plant Pathology*, vol. 19, no. 4, pp. 786–800, 2018.

[5] K. Schneider *et al.*, "Impact of Xylella Fastidiosa Subspecies Pauca in European Olives", *Proceedings of the National Academy of Sciences*, vol. 117, no. 17, pp. 9250–9259, 2020.

[6] J. A. Navas-Cortés *et al.*, "Spatiotemporal Analysis of Spread of Infections by Verticillium Dahliae Pathotypes within a High Tree Density Olive Orchard in Southern Spain", *Phytopathology*, vol. 98, no. 2, pp. 167–180, 2008.

[7] R. Calderón, J. A. Navas-Cortés, C. Lucena, and P. J. Zarco-Tejada, "High-Resolution Airborne Hyperspectral and Thermal Imagery for Early Detection of Verticillium Wilt of Olive using Fluorescence, Temperature and Narrow-Band Spectral Indices", *Remote Sensing of Environment*, vol. 139, pp. 231–245, 2013.

[8] R. Calderon, C. Lucena, J. L. Trapero-Casas, P. J. Zarco-Tejada, and J. A. Navas-Cortes, "Soil Temperature Determines the Reaction of Olive Cultivars to Verticillium Dahliae Pathotypes", *PLoS One*, vol. 9, no. 10, e110664, 2014.

[9] R. Calderón, J. A. Navas-Cortés, and P. J. Zarco-Tejada, "Early Detection and Quantification of Verticillium Wilt in Olive using Hyperspectral and Thermal Imagery over Large Areas", *Remote Sensing*, vol. 7, no. 5, pp. 5584–5610, 2015.

[10] T. Poblete *et al.*, "Discriminating Xylella Fastidiosa from Verticillium Dahliae Infections in Olive Trees using Thermal- and Hyperspectral-Based Plant Traits", *ISPRS Journal of Photogrammetry and Remote Sensing*, vol. 179, pp. 133–144, 2021.

[11] T. Poblete *et al.*, "Detection of Symptoms Induced by Vascular Plant Pathogens in Tree Crops using High-Resolution Satellite Data: Modelling and Assessment with Airborne Hyperspectral Imagery", *Remote Sensing of Environment*, vol. 295, p. 113 698, 2023.

[12] C. Camino *et al.*, "Detection of Xylella Fastidiosa in Almond Orchards by Synergic Use of an Epidemic Spread Model and Remotely Sensed Plant Traits", *Remote Sensing of Environment*, vol. 260, p. 112 420, 2021.

[13] P. Bonants *et al.*, "Development and Evaluation of a Triplex TaqMan Assay and Next-Generation Sequence Analysis for Improved Detection of Xylella in Plant Material", *Plant Disease*, vol. 103, no. 4, pp. 645–655, 2019.

[14] R. Calderón, M. Montes-Borrego, B. Landa, and P. Zarco-Tejada, "Detection of Downy Mildew of Opium Poppy using High-Resolution Multi-Spectral and Thermal Imagery Acquired with an Unmanned Aerial Vehicle", *Precision Agriculture*, vol. 15, no. 6, pp. 639–661, 2014.

[15] R. Calderón Madrid, J. A. Navas Cortés, C. Lucena León, and P. J. Zarco-Tejada, "High-Resolution Hyperspectral and Thermal Imagery Acquired from UAV Platforms for Early Detection of Verticillium Wilt using Fluorescence, Temperature and Narrow-Band Indices", in *Proc of the Workshop on UAV-based Remote Sensing Methods for Monitoring Vegetation*, Transregional Collaborative Research Centre 32, 2013.

[16] B. Efron and R. J. Tibshirani, *An introduction to the bootstrap*. Chapman and Hall/CRC, 1994.

[17] C. Figuera *et al.*, "Nonparametric Model Comparison and Uncertainty Evaluation for Signal Strength Indoor Location", *IEEE Transactions on Mobile Computing*, vol. 8, no. 9, pp. 1250–1264, 2009.

[18] T. Poblete *et al.*, "Detection of Xylella Fastidiosa Infection Symptoms with Airborne Multispectral and Thermal Imagery: Assessing Bandset Reduction Performance from Hyperspectral Analysis", *ISPRS Journal of Photogrammetry and Remote Sensing*, vol. 162, pp. 27–40, 2020.

[19] A. J. McElrone, J. L. Sherald, and I. N. Forseth, "Interactive effects of water stress and xylem-limited bacterial infection on the water relations of a host vine", *Journal of Experimental Botany*, vol. 54, no. 381, pp. 419–430, 2003.

Corn Tassel Emergence Identification and Height Mesurment Based on Unmanned Aerial Vehicles

Junfeng Ma*, Dongliang Chu†, Xukang Lyu†, Aiqin Hou‡, Leping Feng‡, Xu Wang‡, Chase Wu§
* Xinxiang Agricultural Science and Technology Institute
Xinxiang, Henan, 453000, China
E-mail: junfeng816@126.com
† Research and Development Center, Zhejiang Newrise Digital Technology Co.
Hangzhou, Zhejiang, 310056, China
E-mail: {chudongliang,clew}@newrisedt.com
‡ School of Computer Science, Northwest University
Xi'an, Shaanxi, 710127, China
Email: houaiqin@nwu.edu.cn, {fengleping, wangxu1}@stumail.nwu.edu.cn
§ Department of Data Science, New Jersey Institute of Technology
Newark, NJ 07102, USA
Email: chase.wu@njit.edu
Corresponding author: Aiqin Hou (houaiqin@nwu.edu.cn)

***Abstract*—In breeding test fields, where tens or even hundreds of thousands of corns are planted, measurements of numerous phenotypic traits—such as plant height, tassel height, stem thickness, fruiting characteristics (e.g., tassel length, tassel width, awnless tip, row number), disease resistance, and lodging resistance—are typically required. Traditional methods rely on pen-and-paper recordings or basic spreadsheets, which are highly inefficient and prone to human errors, including serial mistakes and incorrect data entries. This makes it difficult to ensure data accuracy and quality. To address these challenges, this paper explores the use of Unmanned Aerial Vehicles (UAVs) and deep learning technologies to monitor the entire growth process of corn plants throughout their life cycle and select high-quality seedlings. Using experiments conducted in corn fields in Henan Province as a case study, the research focuses on identifying the growth and development stages of corn plants, as well as monitoring the timing of tassel emergence. A high-quality dataset covering the entire growth and development process is constructed. Based on UAV remote sensing images with Real-Time Kinematic (RTK) coodinates and timestamps, and 3D point cloud coordinates, we employ You Only Look Once (YOLO)v8 to conduct object detection to accurately identify tassel emergence times during growth. We also collect images of mature corn plants and their point clouds to calculate the height of each mature corn. These approachs aim to achieve precise monitoring of corn growth conditions and facilitate the digital and precise management of the corn cultivation process.**

***Keywords*-Unmanned Aerial Vehicles (UAVs), Real-Time Kinematic (RTK), Deep Learning (DL), You Only Look Once (YOLO).**

I. INTRODUCTION

The growth and development of corn are critical factors influencing both yield and quality. Currently, crop growth monitoring primarily relies on manual sampling, which struggles to meet the demands of modern agriculture for precision and automation. In recent years, the rapid advancements in UAV remote sensing technology and deep learning have opened new possibilities for breakthroughs in crop growth monitoring [1]. UAVs have a wide range of potential applications in agriculture, including reducing manual labor and enhancing productivity. Drones are extensively used for monitoring crop growth and managing fields. They may also provide early detection of plant diseases, enabling farmers to take preventive measures against costly crop failures [2]. In particular, in scenarios such as seedling cultivation and breeding, it is essential to conduct highly detailed monitoring of each seedling's growth conditions, nutritional status, and pest and disease occurrences.

Drones have become widely used in precision agriculture to capture high-resolution images of crops, offering farmers valuable insights into crop health, growth patterns, nutrient deficiencies, and pest infestations. While several machine learning and deep learning models have been proposed for detecting plant growing status and diseases, their accuracy and computational efficiency still need improvement, especially when working with limited data [3]. The integration of Autonomous Aerial Vehicles (AAVs) has significantly advanced image processing and remote sensing, particularly in the field of precision agriculture [4].

This paper explores how drone technology can be utilized to achieve full-cycle monitoring of corn breeding experimental fields, including detecting and identifying the emergence time of corn tassels and the height of mature corn plants. The goal is to identify corn plants with optimal growth conditions and cultivate superior seeds. The contributions of our work are summarized as follows:

i) RTK point positioning technology is used to accurately analyze and determine the precise location of each corn plant.
ii) A UAV fitted with an H20 camera captures orthographic images of the corn test fields throughout the entire growth period. The pixel coordinates of these images correspond to RTK coordinates, and each image is also time-stamped. We

perform segmentation on these images and use YOLOv8 to detect the tassel (the fluffy structure at the top) status of each plant, along with their positions and emergence times. In our experiments, the identification accuracy reaches 82.5%.

iii) A UAV equipped with an L1 laser camera scans the plot to create a point cloud. The coordinates of the point cloud are then aligned with RTK coordinates in the same projection system. This equipment allows us to capture 3D point clouds and images of mature corn test fields. Based on elevation data from the top point cloud and the root point cloud of a mature corn plant, we can calculate the height of each corn plant.

The remainder of the paper is organized as follows. Section II provides a review of representative studies on digital crop management using UAVs and deep learning technologies. In Section III, we present a set of methods for identifying corn tassel emergence and measuring plant height using UAVs. Section IV details the implementation of our experiments. Finally, we conclude our work in Section V.

II. Related Work

Khan et al. [5] proposed an innovative deep learning framework that employs an encoder-decoder architecture to classify each pixel in drone images into categories such as weed, crop, and others. Effective weed control is crucial for enhancing crop yields. Traditionally, weed management relied heavily on herbicide use, but the indiscriminate application of herbicides poses risks to both crop health and productivity. Fortunately, the advent of advanced technologies like UAVs and computer vision has paved the way for automated and efficient weed control solutions. These technologies leverage drone images to detect and identify weeds with a high degree of accuracy.

Gallo et al. [6] created a weed and crop dataset called the Chicory Plant (CP) dataset and tested state-of-the-art deep learning algorithms for object detection. A total of 12,113 bounding box annotations were generated to identify weed targets (Mercurialis annua) from over 3,000 RGB images of chicory plantations, collected using a UAV system at various stages of crop and weed growth. Deep weed object detection was conducted by applying the latest You Only Look Once version 7 (YOLOv7) on both the CP and publicly available datasets, such as the Lincoln Beet (LB) dataset, which previously used an earlier version of YOLO for mapping weeds and crops.

Wu et al. [7] leveraged drone remote sensing data combined with deep object detection models, specifically employing the YOLO-v3 algorithm based on loss function optimization, for the efficient and accurate detection of tree diseases and pests. Utilizing drone-mounted cameras, the study captures insect pest image information in pine forest areas, followed by segmentation, merging, and feature extraction processing. The computing system of airborne embedded devices is designed to ensure detection efficiency and accuracy. The improved YOLO-v3 algorithm combined with the CIoU (Complete Intersection over Union) loss function was used to detect forest pests and diseases. Compared to the traditional IoU loss function, CIoU takes into account the overlap area, the distance between the center of the predicted frame and the actual frame, and the consistency of the aspect ratio.

Deng et al. [8] proposed an end-to-end Global-Local Self-Adaptive Network (GLSAN), in order to address the Object detection from a drone's perspective due to the blurriness of small-scale objects and inefficient detection in areas with uneven or dense object distribution. The key components in their GLSAN include a global-local detection network (GLDN), a simple yet efficient self-adaptive region selecting algorithm (SARSA), and a local super-resolution network (LSRN). They integrate a global-local fusion strategy into a progressive scale-varying network to perform more precise detection, where the local fine detector can adaptively refine the target's bounding boxes detected by the global coarse detector via cropping the original images for higher-resolution detection.

Lan et al. [9] proposed a rice spike detection method that integrates deep learning algorithms with drone-based perspectives. Building on an enhanced version of YOLOv5, the method introduces an Efficient Multiscale Attention (EMA) mechanism, designs a novel neck network structure, and incorporates SCYLLA Intersection over Union (SIoU). The results demonstrate that this approach enables real-time, efficient, and accurate detection and counting of rice spikes in field environments.

Hosseiny et al. [10] proposed an automated and fully unsupervised framework for plant detection in agricultural lands using very high-resolution drone remote sensing imagery. The core idea is to automatically generate an unlimited amount of simulated training data from the input images, which addresses the common limitation of deep learning methods—requiring large amounts of training data. This framework is based on a Faster Regional Convolutional Neural Network (R-CNN) with a ResNet-101 backbone for object detection. The framework's efficiency was evaluated on two different image sets from cornfields, captured using an RGB camera mounted on a drone.

Mota et al. [11] created a database of aerial RGB images of corn crops in weedy conditions to implement and evaluate deep learning algorithms for detecting and counting corn plants.

Kusumo et al. [12] investigated several image-processing-based features for detecting diseases in corn. They examined various features, such as RGB color, local image features like Scale-Invariant Feature Transform (SIFT), Speeded Up Robust Features (SURF), and Oriented FAST and Rotated BRIEF (ORB), as well as object detectors like Histogram of Oriented Gradients (HOG). They evaluated the performance of these features on several machine learning algorithms, including Support Vector Machines (SVM), Decision Tree (DT), Random Forest (RF), and Naive Bayes (NB). Experimental results indicated that RGB color features were the most informative for this task.

Quan et al. [13] presented an improved Faster R-CNN model for a field robot platform (FRP) designed to automatically extract image features and detect maize seedlings quickly and accurately during different growth stages in complex field

environments, with the goal of enabling intelligent inter-tillage in maize fields. The FRP, equipped with five industrial USB cameras, captured a large number of sample images from a 0–90° shooting angle range. These images were used to create a database containing 20,000 images of soil, maize, and weeds. Ten pretrained networks were used to replace the network in the CNN feature-computing component of the classic Faster R-CNN. The proposed method, a Faster R-CNN with VGG19 processed by pretrained networks, was developed for this purpose.

Velumani et al. [14] explored the impact of image ground sampling distance (GSD) on maize plant detection performance at the three-to-five leaf stage using the Faster-RCNN object detection algorithm. The Faster-RCNN model achieved excellent plant detection and counting performance (rRMSE = 0.08) when trained and validated with native high-resolution images. Similarly, good performance (rRMSE = 0.11) was observed when the model was trained on synthetic low-resolution images, obtained by downsampling the native high-resolution images, and applied to synthetic low-resolution validation images. However, poor performance was seen when the model was trained on one spatial resolution and applied to another. Training on a mix of high- and low-resolution images resulted in very good performance on both native high-resolution images (rRMSE = 0.06) and synthetic low-resolution images (rRMSE = 0.10).

Cho et al. [15] proposed a real-time measurement system for obtaining precise target-plant growth information in precision agriculture. They used a smart farm robot that accurately measures plant growth by utilizing object detection, image fusion, and data augmentation with fused images. The system employed image fusion using both RGB and depth images to distinguish the target plant from surrounding plants.

Ahangir et al. [4] addressed the challenge of accurately quantifying corn production by developing an enhanced YOLOv8-based deep learning model, which integrates dynamic and fixed labeling techniques. The model was tested on 810 images and video data for real-time detection.

Daraghmi et al. [3] conducted a comparative analysis of three state-of-the-art object detection deep learning models—YOLOv8, RetinaNet, and Faster R-CNN—and their variants, to identify the model with the best performance for high-resolution crop images. Their study highlighted YOLOv8's robustness, speed, and suitability for real-time aerial crop monitoring, especially in data-constrained environments.

In this paper, we focus on using UAVs and deep learning technology to monitor the entire growth process of each corn plant in an experimental field throughout its life cycle, with the goal of selecting high-quality seedlings. We employ RTK technology to determine the position of each corn plant and use the YOLOv8 model to detect the tassels. By unifying point cloud coordinates with RTK coordinates in the same projection system, we facilitate the calculation of the corn plant's height.

III. METHODS

In this section, we will demonstrate the workflows of using drones for corn inspection.

A. Locating the Position of Each Corn Plant with RTK Coordinates

RTK equipment is used to accurately analyze and determine the location of each corn plant. RTK (Real-Time Kinematic) is a global satellite navigation system (GNSS) technology that provides real-time, high-precision positioning. RTK coordinates include two-dimensional positioning data, such as latitude and longitude (e.g., longitude: 113.758619, latitude: 35.445592), offering centimeter- or even millimeter-level accuracy. This technology is widely used in fields like surveying and mapping. In our case, it provides precise coordinate data that serves as a reference for coordinate transformation.

The UAV then captures aerial images of the corn field, which are exported as image files for further analysis.

B. Method for Identification of Corn Tassel

1) Capturing Images of Corn Fields at Different Growth Stages for Tassel Emergence Identification

The DJI M300 drone, equipped with RTK and the H20 camera, regularly captures orthographic images of the corn fields. By combining these orthographic images with the RTK coordinates provided by the drone, a direct correspondence between the pixel positions in the images and the RTK coordinates is established. A square frame with a side length of 25 cm is placed at the center of each corn plant, within which the tasseling status of the plant is detected, along with its position—specifically, the pixel coordinates of the root and top of the corn plant. It is important to note that these images include both a timestamp and the RTK coordinates of the pixel positions.

2) Identification of Corn Tassels

We construct a high-quality dataset by collecting images from test fields that cover the entire growth and development process of corn plants. Image segmentation and object detection are performed using YOLOv8 to identify the male tassel of corn. YOLOv8 is a hierarchical, multi-scale feature extraction and fusion network. It supports not only object detection but also instance segmentation. Known for its robustness, speed, and suitability for real-time aerial crop monitoring, YOLOv8 is particularly effective in data-constrained environments [3].

First, we perform image segmentation on the collected test field images. We extract the pixels of each corn from an image, which is a square frame with a side length of 25 cm centered on the corn plant's center, and serves as the detection frame of the corn.

Next, YOLOv8 is used to identify the male tassel of the corn. The human visual system employs a selective attention mechanism that automatically focuses on key areas of a scene. Integrating this attention mechanism into a recurrent neural network can significantly enhance image classification performance and improve the model's ability to accurately identify multiple types of targets. Based on this principle, the

Convolution Block Attention Module (CBAM) is integrated into YOLOv8's feature extraction network.

When detecting the male tassel of corn, it is labeled as "tassel" along with a timestamp.

C. Calculation of Corn Plant Height

1) Capturing Images of Corn Field During the Mature Period for Corn Plant Height Calculation

To calculate the height of corn plants, the DJI M300 drone, equipped with a laser radar (L1), captures images of mature corn plants along with point cloud coordinates in local coordinates.

The 3D point cloud coordinates are represented as (x, y, z). Additionally, these images include pixel-to-RTK coordinate correspondence, which helps in locating the position of each corn plant and recording the timestamp when the images are taken.

Two key points need to be marked on each corn plant: the "root" (the base of the stem close to the ground) and the "tip" (the top of the male spike or the highest point of the plant). The pixel coordinates of the tip are crucial for height measurement.

It is particularly important to note that the local point cloud coordinates (x, y, z) must be aligned with the RTK coordinates in the same global coordinate system in order to accurately locate each corn plant and calculate its height. The coordinate conversion method is detailed in the next subsection.

2) Unifying Point Cloud and RTK Coordinates into a Global Coordinate System

First, we unify the point cloud coordinates and RTK coordinates into the same projection coordinate system.

A point cloud is a data set consisting of a large number of points, each containing information such as three-dimensional coordinates (x, y, z) in space. Point clouds can be used to represent the three-dimensional shape and spatial distribution of objects. In this paper, point clouds are utilized to obtain the 3D spatial information of target objects, such as corn plants, for tasks like coordinate transformation and stem height calculation.

The conversion formula, using a seven-parameter model, is employed to convert the local coordinates of the point clouds (x, y, z) into global coordinates (X, Y, Z), as follows:

$$\begin{bmatrix} X \\ Y \\ Z \end{bmatrix}_{\text{global}} = \begin{bmatrix} \Delta X \\ \Delta Y \\ \Delta Z \end{bmatrix} + (1+k) \cdot \boldsymbol{R} \cdot \begin{bmatrix} x \\ y \\ z \end{bmatrix}_{\text{local}}, \quad (1)$$

where $\begin{bmatrix} X & Y & Z \end{bmatrix}^\top$ stands for global coordinates, $\begin{bmatrix} x & y & z \end{bmatrix}^\top$ stands for local coordinates of point cloud, $\begin{bmatrix} \Delta X & \Delta Y & \Delta Z \end{bmatrix}^\top$ is a translation vector, used to represent the position offset transformation model formula for the origin of the local coordinate system in the global coordinate system, k represents the scaling factor, and $\boldsymbol{R}$ represents a rotation matrix:

$$\boldsymbol{R} = \boldsymbol{R}_Z(\omega) \cdot \boldsymbol{R}_Y(\phi) \cdot \boldsymbol{R}_X(\kappa), \quad (2)$$

$$\boldsymbol{R}_X(\kappa) = \begin{bmatrix} 1 & 0 & 0 \\ 0 & \cos\kappa & -\sin\kappa \\ 0 & \sin\kappa & \cos\kappa \end{bmatrix}, \quad (3)$$

$$\boldsymbol{R}_Y(\phi) = \begin{bmatrix} \cos\phi & 0 & \sin\phi \\ 0 & 1 & 0 \\ -\sin\phi & 0 & \cos\phi \end{bmatrix}, \quad (4)$$

$$\boldsymbol{R}_Z(\omega) = \begin{bmatrix} \cos\omega & -\sin\omega & 0 \\ \sin\omega & \cos\omega & 0 \\ 0 & 0 & 1 \end{bmatrix}. \quad (5)$$

3) Method for Calculating Corn Height

Plant height refers to the vertical distance from the root to the top of a corn plant. At the center of each corn plant, a square frame with a side length of 25 cm is placed. The highest point in the point cloud within this frame is detected as the center elevation of the plant, which corresponds to the "tip"—the top of the male spike or the highest point of the plant. The base of the stem, close to the ground, is defined as the "root." Therefore, the height of the corn plant is calculated as the difference between the global coordinates of the tip and the root.

The formula for calculating the actual height of the corn plant is as follows:

$$\boldsymbol{Height} = \boldsymbol{Z}_{tip} - \boldsymbol{Z}_{root}, \quad (6)$$

where Z_{tip} represents the elevation of the tip's coordinates of the corn in the global coordinate system, and Z_{root} represents the elevation of the root's coordinates of the corn in the global coordinate system.

IV. Implementation and Case Study

In this section, we describe our experiments conducted in corn breeding test fields in Xinxiang, Henan Province, using the DJI M300 drone equipped with various devices and cameras to capture images for different purposes.

A. Locating Corn Plants with RTK

RTK equipment is used to accurately analyze and determine the location of each corn plant in the test fields of Xinxiang, Henan Province.

For example, Figure 1 (a) and (b) show two corn seedlings, each marked with their respective RTK coordinates.

B. Identification of Corn Tassel

The DJI M300 drone, equipped with the H20 camera, captures orthographic images of cornfields. By combining these orthographic images with the RTK coordinates, a correspondence between the pixel positions in the images and the RTK coordinates is established.

We collected 1,000 images taken in corn test fields in Xinxiang, Henan Province, at fixed intervals (i.e., every three days) throughout the entire growth period, using the DJI M300 drone. A correspondence between the pixel positions in the images and the RTK coordinates is established. These images, captured by the drone, are marked with both RTK coordinates and time stamps.

At the center of each corn plant, a square frame with a side length of 25 cm is placed, and the tasseling status of each

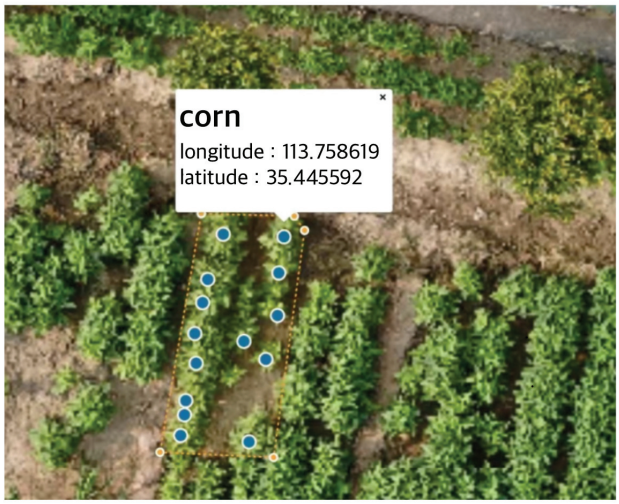

(a) RTK1

(b) RTK2

Figure 1: Corn plants with RTK coordinates.

Figure 2: Photo of corn plants.

plant within the frame is detected, along with their positions and timestamps.

Figure 2 shows a corn plant with its male tassel spike emerging. The image clearly reveals the main axis of the male spikelet and several male spikelet branches.

The detection model we used is the deep learning-based YOLOv8 (medium) network, which is applied to these images to identify the corn tassels.

First, we perform image segmentation on the collected test field images. We extract the pixels of each corn from an image, defining a square frame with a side length of 25 cm centered on the middle of each corn plant, which serves as the detection frame for the plant.

We used 810 images for the training set and 190 images for the test set. The corn tassel at each plant position within the detection frame is detected. The test results show that the accuracy rate can reach 82.5%. This demonstrates the effectiveness of YOLOv8 in capturing fine plant features under real field conditions, while also indicating that further optimization of parameters and training data could yield even higher detection performance.

C. Calculatiion Corn Height

The DJI M300 drone is equipped with an L1 laser camera that scans the plot to generate a 3D point cloud. The point cloud coordinates are then aligned with the RTK coordinates within the same projection coordinate system. At the center of each corn plant, a square frame with a side length of 25 cm is placed, within which the highest point cloud elevation is detected, serving as the plant's center elevation.

Figure 3 shows three corn plants in a field, with the global coordinates of their respective 3D point clouds. The points marked in the figure represent the highest point of each corn plant's point cloud, enclosed by the 25 cm frame.

For example, Figure 4 shows an image of a mature corn test field, highlighting a corn plant with the global coordinates of its tip and root, represented by three-dimensional point clouds.

As shown in the figure, the tip and root of a mature corn plant share the same longitude and latitude coordinates, but their elevation coordinates differ. The elevation coordinates of the tip and root are 66.911 m and 64.602 m, respectively, with the unit defaulted to the international standard of meters.

Based on the coordinate values marked in Figure 4, and using Eq. (6) from Section III-C3, we can calculate the height of this corn plant as follows: 66.911 - 64.602 = 2.309 m.

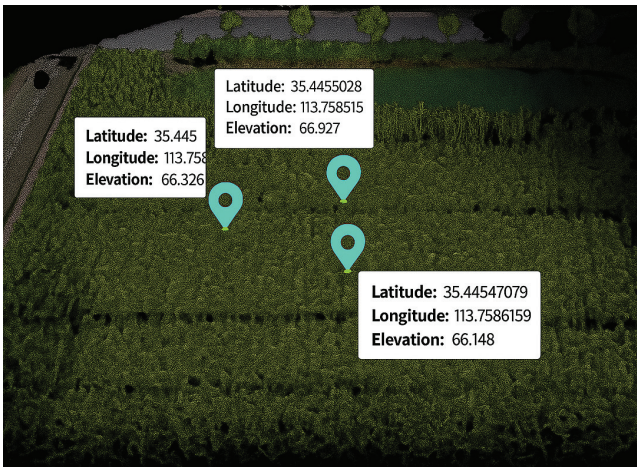

Figure 3: Photo with three global point cloud coordinates.

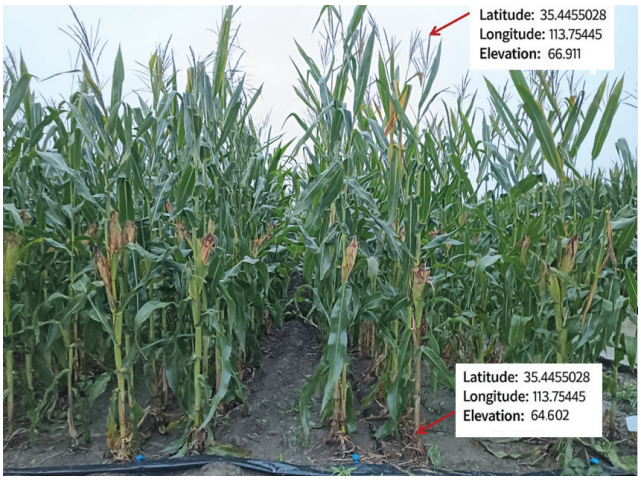

Figure 4: Photo with tip and root point cloud coordinates of corn plants.

This straightforward calculation confirms the vertical growth measurement method and provides a reliable reference for evaluating plant height across the test field.

V. Conclusion And Future Work

In this study, we proposed and validated an integrated framework that combines UAV imagery and deep learning techniques to monitor tassel emergence timing and plant height in corn breeding fields. By leveraging high-resolution drone images, precise RTK positioning, YOLOv8-based tassel detection, and 3D point cloud analysis, we achieved accurate and automated extraction of critical agronomic traits at the single-plant level. This approach not only reduces the labor intensity and potential errors associated with manual measurements but also provides efficient data support for large-scale breeding trials, thereby improving the efficiency of high-quality germplasm selection.

However, the relatively small dataset may limit generalizability, and the evaluation relied mainly on accuracy; future work should include precision, recall, and F1 score for a more complete assessment. We also plan to expand monitoring to traits such as tassel height, stem thickness, and fruiting characteristics, and to integrate multi-source data with advanced models to enhance robustness. Overall, this work provides a practical foundation for UAV-based phenotyping and highlights directions for future improvement.

References

[1] J. Li, F. Pu, H. Chen, X. Xu, and Y. Yu, "Crop segmentation of unmanned aerial vehicle imagery using edge enhancement network", *IEEE Geoscience and Remote Sensing Letters*, vol. 21, pp. 1–5, 2024.

[2] A. Abbas *et al.*, "Drones in plant disease assessment, efficient monitoring, and detection: A way forward to smart agriculture", *Agronomy*, vol. 13, no. 6, 2023, ISSN: 2073-4395.

[3] Y.-A. Daraghmi, W. Naser, E. Y. Daraghmi, and H. Fouchal, "Drone-assisted plant stress detection using deep learning: A comparative study of yolov8, retinanet, and faster r-cnn", *AgriEngineering*, vol. 7, no. 8, 2025.

[4] A. Jahangir Moshayedi *et al.*, "Smart farming solutions: A user-friendly gui for maize tassel estimation using yolo with dynamic and fixed labelling, featuring video support", *IEEE Access*, vol. 13, pp. 57 809–57 833, 2025.

[5] S. D. Khan, S. Basalamah, and A. Lbath, "Weed–crop segmentation in drone images with a novel encoder–decoder framework enhanced via attention modules", *Remote Sensing*, vol. 15, no. 23, 2023, ISSN: 2072-4292.

[6] I. Gallo *et al.*, "Deep object detection of crop weeds: Performance of yolov7 on a real case dataset from uav images", *Remote Sensing*, vol. 15, no. 2, 2023, ISSN: 2072-4292.

[7] Y. Wu, H. Yang, and Y. Mao, "Detection of the pine wilt disease using a joint deep object detection model based on drone remote sensing data", *Forests*, vol. 15, no. 5, 2024, ISSN: 1999-4907.

[8] S. Deng *et al.*, "A global-local self-adaptive network for drone-view object detection", *IEEE Transactions on Image Processing*, vol. 30, pp. 1556–1569, 2021.

[9] M. Lan *et al.*, "Rice-yolo: In-field rice spike detection based on improved yolov5 and drone images", *Agronomy*, vol. 14, no. 4, 2024, ISSN: 2073-4395.

[10] B. Hosseiny, H. Rastiveis, and S. Homayouni, "An automated framework for plant detection based on deep simulated learning from drone imagery", *Remote Sensing*, vol. 12, no. 21, 2020, ISSN: 2072-4292.

[11] C. Mota-Delfin, G. d. J. López-Canteñs, I. L. López-Cruz, E. Romantchik-Kriuchkova, and J. C. Olguín-Rojas, "Detection and counting of corn plants in the presence of weeds with convolutional neural networks", *Remote Sensing*, vol. 14, no. 19, 2022, ISSN: 2072-4292.

[12] B. S. Kusumo, A. Heryana, O. Mahendra, and H. F. Pardede, "Machine learning-based for automatic detection of corn-plant diseases using image processing", in *2018 International Conference on Computer, Control, Informatics and its Applications (IC3INA)*, 2018, pp. 93–97.

[13] L. Quan *et al.*, "Maize seedling detection under different growth stages and complex field environments based on an improved faster r–cnn", *Biosystems Engineering*, vol. 184, pp. 1–23, 2019, ISSN: 1537-5110.

[14] K. Velumani *et al.*, "Estimates of maize plant density from uav rgb images using faster-rcnn detection model: Impact of the spatial resolution", *Plant Phenomics*, vol. 2021, p. 9 824 843, 2021, ISSN: 2643-6515.

[15] S. Cho *et al.*, "Plant growth information measurement based on object detection and image fusion using a smart farm robot", *Computers and Electronics in Agriculture*, vol. 207, p. 107 703, 2023, ISSN: 0168-1699.